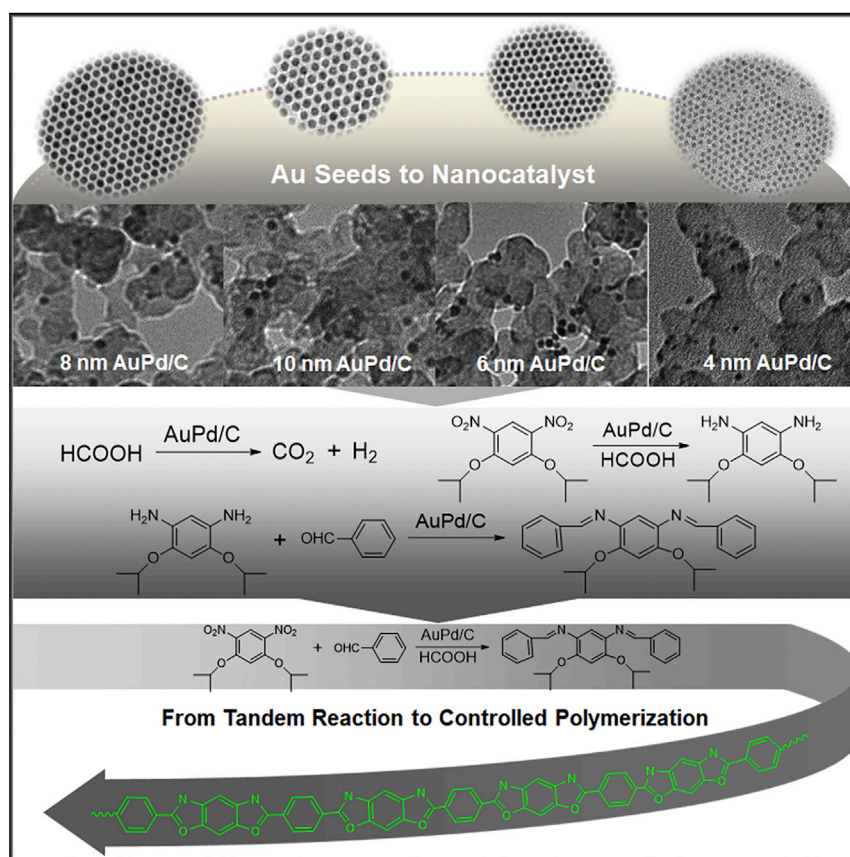


Article

Highly Efficient AuPd Catalyst for Synthesizing Polybenzoxazole with Controlled Polymerization



Chao Yu, Xuefeng Guo,
Zhouyang Yin, ..., Pradeep
Guduru, Christopher T. Seto,
Shouheng Sun

christopher_seto@brown.edu (C.T.S.)
ssun@brown.edu (S.S.)

HIGHLIGHTS

Establishes a controllable seed-mediated growth of AuPd nanoparticles

Builds a relationship between the sizes of nanocatalyst and macroscopic product

Develops a heterogeneous and stable nanomaterial for tandem polycondensation

Offers a greener synthesis to solve the practical hydrolysis problem of Zylon

Metal nanoparticles (NPs) have been extensively studied as heterogeneous catalysts for chemical reactions of small molecules. However, using these NPs to catalyze multi-component reactions into complex molecular structures, for example, polymers, has been rarely reported. We demonstrate a size-dependent catalysis of AuPd alloy NPs for synthesizing highly pure rigid organic polymer polybenzoxazole (PBO) with controlled polymerization in a one-pot reaction condition. The PBO shows the enhanced thermal, chemical, and mechanical stability under challenging environmental conditions.



Discovery

A new material or phenomena

Yu et al., Matter 1, 1631–1643
December 4, 2019 © 2019 Elsevier Inc.
<https://doi.org/10.1016/j.matt.2019.09.001>



Article

Highly Efficient AuPd Catalyst for Synthesizing Polybenzoxazole with Controlled Polymerization

Chao Yu,^{1,5} Xuefeng Guo,^{1,5} Zhouyang Yin,¹ Zhonglong Zhao,² Xing Li,³ Jerome Robinson,¹ Michelle Muzzio,¹ Cintia J. Castilho,⁴ Mengqi Shen,¹ Yucheng Yuan,¹ Junyu Wang,¹ John Antolik,⁴ Gang Lu,² Dong Su,³ Ou Chen,¹ Pradeep Guduru,⁴ Christopher T. Seto,^{1,*} and Shouheng Sun^{1,6,*}

SUMMARY

Using nanoparticles (NPs) to catalyze chemical reactions for the formation of functional polymers with controlled polymerization is an important field of chemical research. In this article, we report an AuPd NP system as an active and stable catalyst to catalyze one-pot reaction of formic acid, 1,5-diisopropoxy-2,4-dinitrobenzene, and terephthalaldehyde, leading to the controlled polymerization and the formation of polybenzoxazole (PBO) ($M_w = 3.6$ kDa). The one-pot reaction is AuPd NP size and composition dependent, and 8-nm $Au_{39}Pd_{61}$ NPs are the best catalyst for the polymerization. The highly pure PBO shows excellent thermal stability up to 600°C and improved chemical and mechanical stability under challenging environmental conditions compared with commercial PBO (Zylon, $M_w = 40$ kDa). The reported NP-catalyzed one-pot reaction to polymerization is not limited to the formation of PBO but can be extended as a general approach to rigid polymers that are important for ballistic fiber, anti-flame, and smart-textile applications.

INTRODUCTION

Advances in nanoparticle (NP) synthesis have motivated extensive research into defining the “tuning knobs” that can be used to control the physical and chemical properties of NPs.^{1–8} One of these properties is catalysis. Various NPs, especially metallic NPs, have been explored as efficient catalysts to promote chemical reactions in much milder and greener reaction conditions, which have recently been highlighted extensively in reactions such as water splitting, hydrogen evolution reaction, oxygen reduction reaction, and CO₂ reduction.^{9–15} Some of the noble metal NPs based on Pt, Pd, Ru, Au, and Ag are of special interest in catalyzing miscellaneous organic functionalization reactions due to their desired activity and stability.^{16–25} The preparation of monodisperse NPs further allows the NP catalysis to be tuned in a size-, structure-, and morphology-dependent manner, making it possible to optimize NP catalysis for chemical reactions. However, these previous studies on NP catalysis focus nearly exclusively on chemical reactions to small organics and very rarely on multi-component reactions that lead to the formation of functional materials, for example, polymers, under green chemistry reaction conditions.

Controlling the degree of polymerization is an essential step in obtaining polymer materials with desired macroscopic chemical and physical properties for various applications. Conventional syntheses rely on reactions among monomers under

Progress and Potential

Dimension- and property-controlled nanoparticles (NPs) have become attractive new classes of heterogeneous catalysts for various chemical reactions, especially tandem reactions, by reducing the numbers of reaction steps and by increasing the reaction efficiencies toward targeted products. Here, we report an AuPd NP system as an active and stable catalyst to catalyze one-pot reaction of formic acid, 1,5-diisopropoxy-2,4-dinitrobenzene, and terephthalaldehyde, leading to the controlled polymerization and formation of polybenzoxazole (PBO). The highly pure PBO shows excellent thermal stability up to 600°C and improved chemical and mechanical stability compared with phosphoric acid-contaminated commercial PBO (Zylon, $M_w = 40$ kDa). The reported NP-catalyzed one-pot polymerization can be easily extended to prepare various rigid organic polymers that are important for ballistic fiber, anti-flame, smart-textile, and ionic separation membrane applications.



reaction conditions whereby chain transfer agents are typically needed to control polymerization degrees. These processes have been applied to produce many different kinds of polymers of commercial importance, such as Kevlar, Dacron, Kodel, Lexan, Lycra, and Zylon. Despite the common uses of these conventional methods for polymer productions, the reactions still have issues in rationally controlling the degrees and purities of polymerizations. Here, we report a new process of synthesizing highly pure polybenzoxazole (PBO) with controlled polymerization via AuPd NP-catalyzed one-pot reaction. PBO, or Zylon for the commercial product, is a subclass of polybenzoxazoles. The highly aromatic nature and conjugated structure of alternating benzoxazole and phenyl rings provides the polymer with the highest yarn tensile strength (5.8 GPa), stiffness (270 GPa), and relatively low density ($1.5\text{--}1.7\text{ g cm}^{-3}$) among all commercial synthetic polymers.^{26–29} These characteristics render the polymer with exceptionally superior tensile modulus and strength as well as thermal and mechanical stability, making it a promising new fiber material for applications in body armor, flame retardation, smart electronic textiles, and ionic separation membranes.^{30–33} However, PBOs are conventionally made by condensing diaminobenzene diol and terephthalic acid with polyphosphoric acid as both solvent and catalyst. As a result, they are inevitably contaminated with phosphoric acid (PA) units that can catalyze the hydrolysis of the benzoxazole ring upon its exposure to humid and lighted environments (Figure S1), causing unexpected and fast degradation of the mechanical integrity of the polymer fibers.^{34–36} Our new AuPd NP-catalyzed one-pot reaction of formic acid, 1,5-diisopropoxy-2,4-dinitrobenzene, and terephthalaldehyde to PBO is NP size- and composition-dependent, and among the 4-, 6-, 8-, and 10-nm AuPd NPs studied, 8-nm Au₃₉Pd₆₁ NPs are the most efficient in catalyzing the reaction to the highest degree of polymerization (molecular weight [M_w] = 3.6 kDa). Compared with the Zylon (M_w = 40 kDa), our “lighter” PBO has not only comparable thermal stability (over 600°C) but also much improved chemical and mechanical stability against water- and organic-solvent-induced polymer degradation. Molecular mechanics (MM) and density functional theory (DFT) simulations reveal that both surface strain and surface geometry of the AuPd NPs contribute to the size-dependent polymerization. Our studies show a general approach to NP-controlled catalysis applied to polymerization.

RESULTS AND DISCUSSION

Recently, AuPd alloy NPs were studied as stable catalysts to dehydrogenate formic acid into H₂ for hydrogenation reactions.^{37–40} These AuPd NPs were previously prepared by co-reduction methods, under which it is difficult to control both sizes and compositions of the NPs. We modified the synthesis and developed a unique seed-mediated growth-diffusion method to prepare AuPd NPs with well-controlled sizes and compositions. In our synthesis, 4-, 6-, 8-, and 10-nm Au NPs were first prepared as described.⁴¹ Then, in the presence of Au seeding NPs, a controlled amount of Pd(acac)₂ was reduced in oleylamine (OAm) and oleic acid (OAc) (v/v = 50:1) at 260°C to yield AuPd NPs (see Supplemental Information). We further deposited these AuPd NPs onto a Ketjen carbon support (C) and annealed the supported NPs, NPs/C, under forming gas at 500°C for 10 min to obtain catalytically active AuPd alloy NPs. Figure 1 shows representative transmission electron microscopy (TEM) images of 8-nm Au seeding NPs (Figure 1A) and 8.2 ± 0.4 nm AuPd/C (Figure 1B) (TEM images of other Au NPs and AuPd NPs are given in Figures S2A–S2C and S3A–S3C, respectively). Starting from 4-, 6-, 8-, and 10-nm Au NPs, we obtained 4.3 ± 0.2 , 6.4 ± 0.3 , 8.2 ± 0.4 , and 10.5 ± 0.2 nm Au₃₉Pd₆₁ alloy NPs, showing a very small NP size increase after the alloy formation. For simplicity of presentation, these AuPd NPs are denoted as 4-, 6-, 8-, and 10-nm NPs in this paper. The alloy

¹Department of Chemistry, Brown University, Providence, RI 02912, USA

²Department of Physics and Astronomy, California State University Northridge, Northridge, CA 91330, USA

³Center for Functional Nanomaterials, Brookhaven National Laboratory, Upton, NY 11973, USA

⁴School of Engineering, Brown University, Providence, RI 02912, USA

⁵These authors contributed equally

⁶Lead Contact

*Correspondence: christopher_seto@brown.edu (C.T.S.), ssun@brown.edu (S.S.)

<https://doi.org/10.1016/j.matt.2019.09.001>

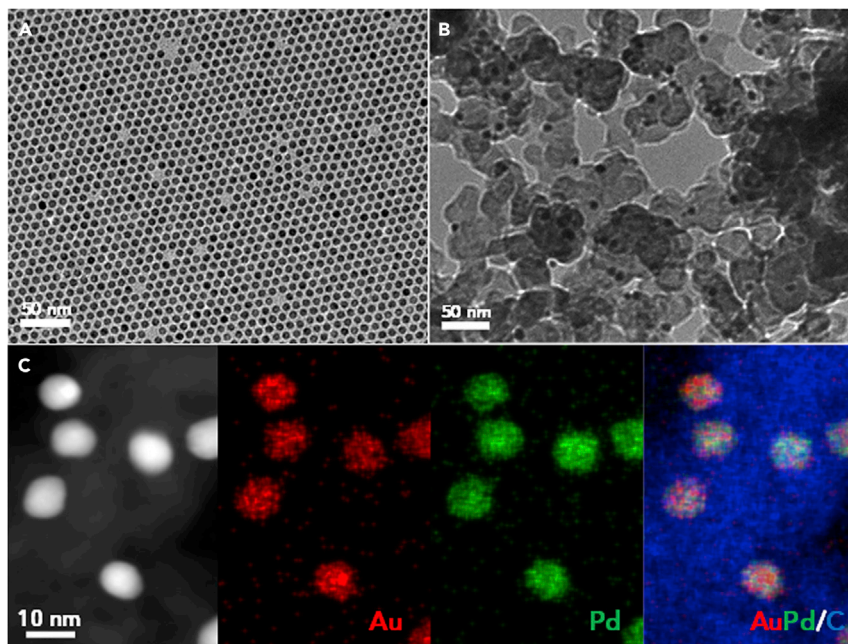


Figure 1. Preparation and Characterization of AuPd Alloy NPs

(A) TEM image of 8-nm Au NPs, scale bar: 50 nm.

(B) TEM image of 8.2 ± 0.4 -nm $\text{Au}_{39}\text{Pd}_{61}$ NPs deposited on (C), scale bar: 50 nm.

(C) HAADF-STEM image of the $\text{Au}_{39}\text{Pd}_{61}/\text{C}$ and elemental mapping of NPs to show Au (red) and Pd (green) distribution within the NPs, scale bar: 10 nm.

structure of the NPs was characterized by high-resolution TEM (HRTEM) (Figure S4), high-angle annular dark field (HAADF) scanning TEM (STEM) and elemental mapping (Figure 1C), X-ray diffraction analysis, and X-ray photoelectron spectroscopy (XPS) (Figures S5–S7 and Table S1). From these analyses, we conclude that homogeneous alloy AuPd NPs with a face-centered cubic structure are obtained.

The controls achieved in preparing AuPd NPs allow us to study size- and composition-dependent catalysis for reactions leading to the formation of small subunits of PBO. In this test, we studied formic acid (FA)-induced reduction of 1,5-diisopropoxy-2,4-dinitrobenzene and the subsequent condensation of the 1,5-diisopropoxy-2,4-aminobenzene product with benzaldehyde to form (1E,1'E)-N,N'-(4,6-diisopropoxy-1,3-phenylene)-bis(1-phenylmethanimine) (denoted as bis-imine) in N-methylpyrrolidone (NMP) solvent (Figure 2A). We attached isopropyl groups to the oxy-nitrobenzene structure to ensure that both reactants and products were soluble.⁴² The results of the AuPd-catalyzed reactions are summarized in Figures 2B and 2C, from which we conclude that 8-nm $\text{Au}_{39}\text{Pd}_{61}$ NPs are the most active catalyst for the reduction/condensation reaction (Figure 2A).

The 8-nm $\text{Au}_{39}\text{Pd}_{61}/\text{C}$ (2.5 mol %) was used to catalyze FA-induced reduction of 1,5-diisopropoxy-2,4-dinitrobenzene and subsequent condensation with terephthalaldehyde in NMP to form poly(*p*-phenylene-(4,6-diisopropoxy-1,3-phenylene)diethanimine), denoted as pre-PBO, which was further subject to heating treatment at 300°C under a N_2 atmosphere for 6 h to remove isopropyl groups and promote ring closure for the formation of PBO (Figure 3). From TEM (Figure S8) and ICP-AES (inductively coupled plasma atomic emission spectroscopy) elemental analyses, we concluded that the NPs have no composition change before and after

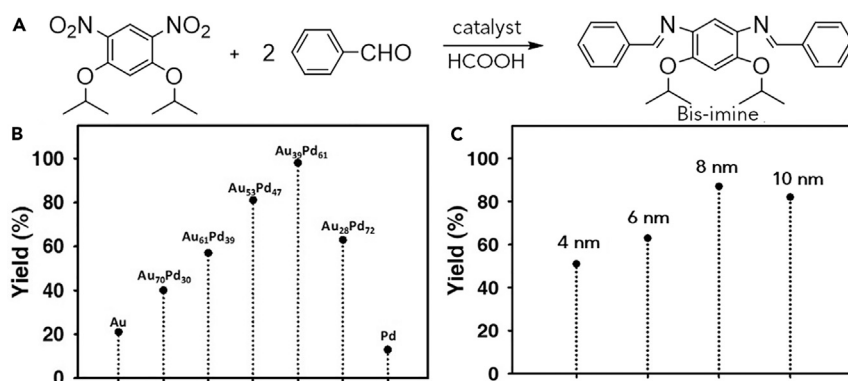


Figure 2. Au₃₉Pd₆₁-Catalyzed Reaction between 1,5-Diisopropoxy-2,4-Dinitrobenzene and Benzaldehyde

(A) A new synthetic route for producing a bis-imine via the condensation of 1,5-diisopropoxy-2,4-dinitrobenzene and benzaldehyde.

(B and C) The yields of bis-imine with different compositions of 8-nm AuPd (B) supported on (C). Reaction conditions: AuPd/C (2.5 mol %), 1,5-diisopropoxy-2,4-dinitrobenzene (1 mmol), benzaldehyde (2.1 mmol), NMP (3 mL), and FA (10 mmol); 80°C, 6 h. (C) The yields of bis-imine with four different sizes of Au₃₉Pd₆₁/C as tandem catalyst. Reaction conditions: Au₃₉Pd₆₁/C (2.5 mol %), 1,5-diisopropoxy-2,4-dinitrobenzene (1 mmol), benzaldehyde (2.1 mmol), NMP (3 mL), and FA (10 mmol); 80°C, 6 h.

polymerization reaction. We further performed cyclic voltammetry (CV) studies of the AuPd catalyst to study NP redox property change, which is sensitive to the NP surface structure. We studied the catalyst CV in 0.5 M H₂SO₄ at a scan rate of 50 mV s⁻¹ in the potential range from 0 V to 1.7 V (versus reversible hydrogen electrode [RHE]) (Figure S9). We can see that the reduction peaks of the oxidized Au (at 1.12 V) and Pd (at 0.55 V) are nearly identical, indicating that there is no surface structure change of the catalyst during the polymerization process. The reduction peak area can be integrated to obtain the Au/Pd composition information, and we see no obvious surface composition change after the polymerization reaction (Table S2). We also studied XPS of the alloy catalyst (Figure S10). We see no obvious Au/Pd binding energy (Figure S10) and atomic percentage change of the catalyst before and after the reaction (Table S2). Summarizing the Au/Pd composition information we obtained from ICP-AES, CV, and XPS (Table S2), we conclude that our AuPd alloy catalyst is not only active but also stable in the polymerization process.

Thermal gravimetric analysis (TGA) under a N₂ atmosphere showed that the pre-PBO has a weight loss of 25.7%, which agrees well with the calculated weight loss of 27.3% for the pre-PBO/PBO conversion (Figure S11). Infrared spectra of the newly prepared PBO show characteristic benzoxazole C=N, C-N, and C-O vibration peaks at approximately 1,620, 1,360, and 1,054 cm⁻¹, respectively, which are similar to that of the commercial PBO, Zylon (Figure S12). UV-visible (UV-vis) absorption spectra taken in methanesulfonic acid solutions of PBO and Zylon show the nearly identical absorption and photoluminescence (PL) peaks (Figure S13), indicating the highly aromatic nature and conjugated structure of alternating benzoxazole and phenyl rings within PBO and Zylon.⁴³ The two split absorption peaks of 404 nm and 428 nm for PBO are induced by intermolecular interactions, consistent with that of the Zylon sample.⁴⁴ A more interesting aspect of this reaction is that the degree of polymerization is dependent on the size of the AuPd NPs. Among 4-, 6-, 8-, and 10-nm AuPd NPs tested, pre-PBO was formed with an *M_w* of 2.1, 2.4, 3.6, and 3.0 kDa, respectively, as measured by gel-permeation chromatography (GPC) (Figure S14A). The 8-nm NPs induced the highest degree of polymerization in the

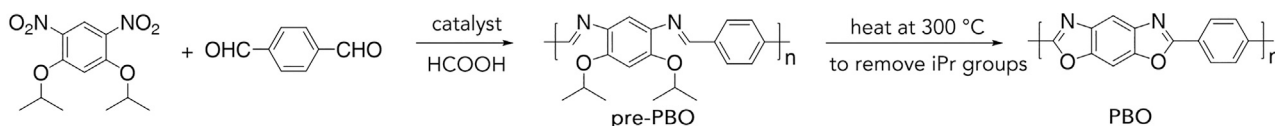


Figure 3. A New Synthetic Route for Producing PBO

one-pot reaction process. The catalyst was also reusable: our preliminary tests show that after three reaction runs, the polymer prepared from each run had similar M_w and the NP catalyst showed no obvious composition and morphology change (Figures S8 and S14B). ICP-AES measurements show that the PBO synthesized using our method is metal- and PA-free. As a comparison, Zylon contains 0.5% (by weight) of P, which means that there is one PA group for every ~ 25 repeating PBO units.

A large concern of PBO-based materials has been its long-term thermochemical and mechanical stability, which has been attributed to accelerated hydrolysis due to residual phosphorus contaminants from the PA used in their synthesis.^{34–36} As the PBO generated through our method is PA-free, it allows us to study for the first time the intrinsic stability properties of this PBO in different environmental conditions. We first performed the TGA of our PBO and the commercial PBO Zylon under a N_2 atmosphere (Figure 4A). Our pristine PBO ($M_w = 3.6$ kDa) displays an onset decomposition temperature at 600°C, whereas Zylon ($M_w = 40$ kDa) has it at 650°C. After immersion in water or DMSO under ambient conditions for 1 month, the onset decomposition temperature for Zylon and PBO were comparable (610°C and 600°C, respectively; Figure 4A). After the samples were immersed in boiling water for 5 days, the onset decomposition temperature of Zylon was reduced to 500°C, while the PBO was still at $\sim 600^\circ\text{C}$ (Figure 4B). The difference in PBO and Zylon thermal stability was also observed in 5% (T_5) and 20% (T_{20}) mass loss temperatures. Zylon displayed a significant depression of T_5 (587°C) and T_{20} (689°C) than the PBO (T_5/T_{20} at 635°C/693°C). To confirm that use of PA in the synthesis can lead to the fast hydrolysis of PBO, we immersed both Zylon and our PBO samples in boiling 0.5% PA aqueous solution for 5 days and then measured their thermal and mechanical properties (Figures 4B and 4C). The onset decomposition temperature of Zylon drops even further to $\sim 450^\circ\text{C}$, while that of the PBO is at $\sim 550^\circ\text{C}$. This PA-induced hydrolysis study supports the notion that the presence of PA can accelerate PBO hydrolysis, and our PA-free PBO made from the one-pot catalytic reaction is more stable against this hydrolysis degradation than the PA-contaminated Zylon. Tensile stress measurements on 7.6- μm -thick PBO and 10.5- μm -thick Zylon films (Figure S15) revealed that the higher M_w Zylon film was stronger prior to environmental challenges (Figure 4C). After immersing the samples in boiling water or boiling 0.5% PA aqueous solution for 5 days, Zylon was subject to a more significant drop in mechanical strength to 15.1 MPa than the PBO film to 21.4 MPa (Figure 4C). Our studies demonstrate that the highly pure PBO, even at a significantly lower degree of polymerization than Zylon, can display improved thermal and mechanical stability after accelerated hydrolysis conditions.

To understand why the catalytic formation of PBO in the one-pot reaction depends on the size of AuPd NPs, we analyzed the model reaction of FA-induced reduction of 1,5-diisopropoxy-2,4-dinitrobenzene and the amine condensation with benzaldehyde (Figure 2A) in three reaction steps: FA dehydrogenation, reduction of the nitro groups, and condensation of the diamine with aldehyde. From the NP size-dependent dehydrogenation of FA (Figure S16A), we can see that the 4-nm NP catalyst provides the highest initial turnover frequency (TOF) value. As the size increases,

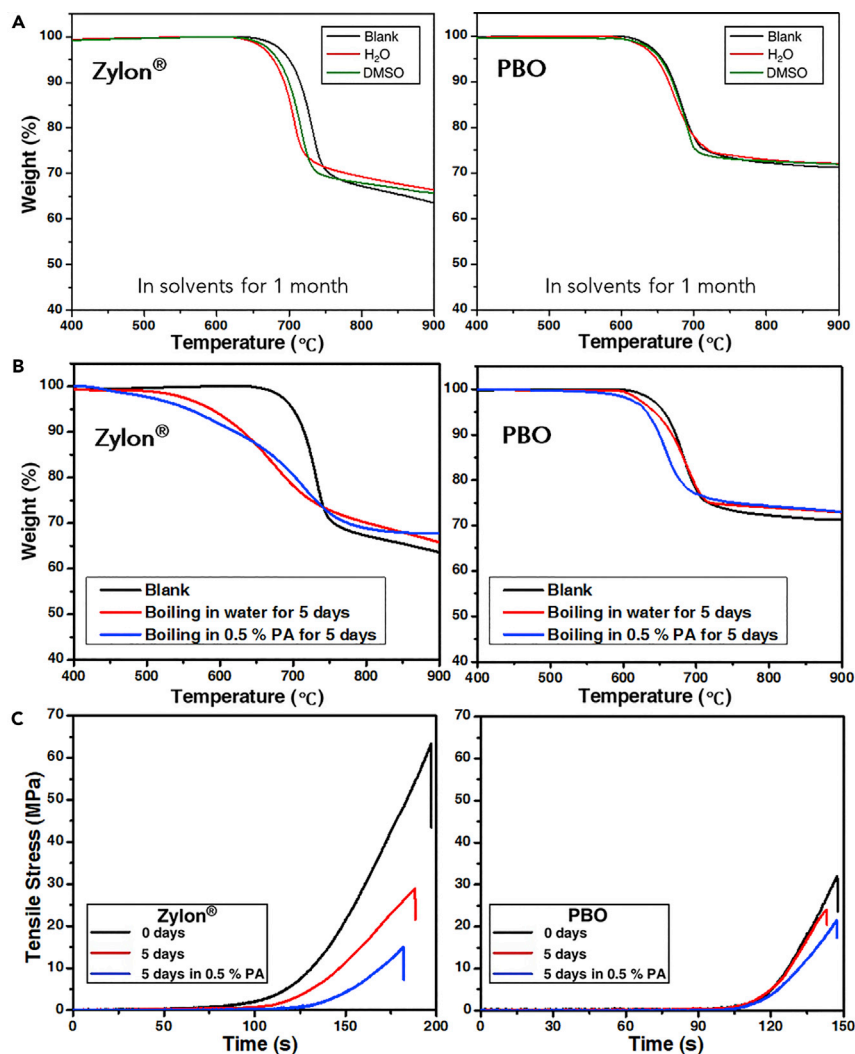


Figure 4. The Thermal Stability and Mechanical Properties of the as-Prepared PBO

(A) TGA data for Zylon and PBO after immersing in H₂O or DMSO at ambient temperature for 1 month.

(B) TGA data for Zylon and PBO after immersing in boiling water and boiling 0.5% PA aqueous solution for 5 days.

(C) Tensile strength of Zylon and PBO as a function of time at a rate of 0.1 mm min⁻¹ before and after immersing in boiling water and boiling 0.5% PA aqueous solution for 5 days.

the activity drops and the TOF decreases from 223 to 170 h⁻¹. A similar trend is observed for the hydrogenation of 1,5-diisopropoxy-2,4-dinitrobenzene (Figure S16B). However, for the condensation of two equivalents of benzaldehyde with 1,5-diisopropoxy-2,4-diaminobenzene, larger NPs (8 and 10 nm) are more efficient, and 8-nm NPs are the best catalyst for the reaction (Figure S16C), which is consistent with what we observed in Figure 2C and in the PBO synthesis. We should clarify here that the presence of AuPd NPs in the reaction solution is essential for the condensation reaction step (Table S3). Without AuPd NPs as the catalyst, the condensation reaction could not proceed smoothly and could only produce the imine product in <35% yield. FA dehydrogenation on metal surfaces has been studied by DFT,⁴⁵ which indicates that H* binds too strongly on pure Pd (111) but too weakly on pure Au (111). Using combined classical MM⁴⁶ and DFT simulations, we

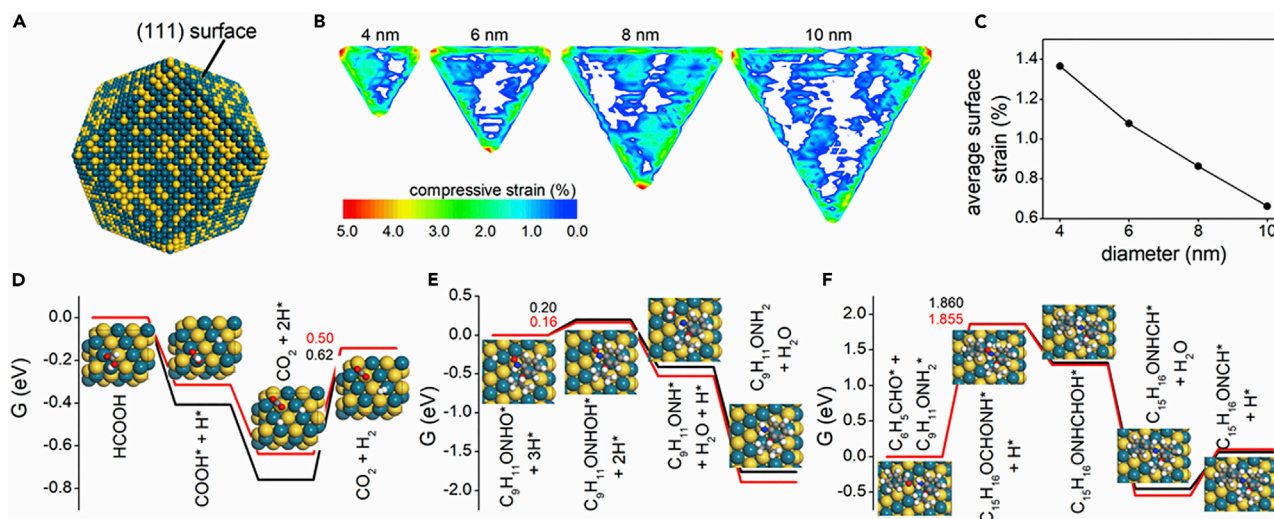


Figure 5. Strain Distributions on the Au₃₉Pd₆₁NPs and Free Energy Diagrams of the Three Reaction Steps

(A) Atomistic model of Au₃₉Pd₆₁ NP.

(B) Color-coded strain distribution on the (111) facets of AuPd NPs with different diameters.

(C) Average surface compression on the NPs as a function of their diameter.

(D) Free energy diagram for the FA dehydrogenation on the (111) surface of the NP under zero strain (black) and 2% compression (red).

(E) Free energy diagram for the hydrogenation of 1,5-diisopropoxy-2,4-dinitrobenzene on the NP under zero (black) and 2% compression (red).

(F) Free energy diagram for the condensation of 1,5-diisopropoxy-2,4-diaminobenzene and benzaldehyde on the NP under zero (black) and 2% compression (red). The adsorption geometries are shown in the insets: yellow, cyan, gray, blue, red, and white spheres represent Au, Pd, C, N, O, and H atoms, respectively.

can elucidate the observed size-dependent polymerization on the AuPd NPs. From the strain distribution on the Au₃₉Pd₆₁ NP (111) surface (Figure 5A), we find that the smaller NPs exhibit a higher degree of compression (Figure 5B), and the average surface compression on 4-, 6-, 8-, and 10-nm Au₃₉Pd₆₁ NPs is 1.37%, 1.08%, 0.86%, and 0.66%, respectively (Figure 5C). The free energy diagrams are calculated to estimate the overpotential for each reaction step (Figures 5D–5F). We find that on an AuPd slab without the compressive strain, the metal surface binds H* too strongly, resulting in a high overpotential of 0.62 V; on an AuPd surface with 2% compression, the overpotential is lowered to 0.5 V. Since 4-nm NPs have the largest surface compression of 1.37%, they should be the most active catalyst for FA dehydrogenation. In the -NO₂ hydrogenation reaction step, migration of surface H* toward O–NO is the only endothermic reaction step (Figure 5E); the surface compression decreases the migration energy barrier and promotes the hydrogenation reaction. Thus, the smaller the NPs (4 nm in the study), the higher the activity. In the condensation reaction step, the formation of the C–N bond is the rate-determining step, which is also enhanced by the surface compression thanks to weakened adsorption of the amino and carbonyl groups (Figure 5F). On the other hand, the condensation reaction involves two large molecules (amine and aldehyde), requiring larger NPs for the reaction (Figure S17). Otherwise, the reactants are too close to the undercoordinated edge sites, lowering the reaction activity (Figure S18).⁴⁷ By taking both strain and geometric factors into consideration, we conclude that 8-nm NPs are the most active for catalyzing the condensation and further polymerization reactions.

Conclusions

We report a new NP-based catalytic approach to synthesize functional polymers with controlled polymerization, purity, and properties. Using the rigid organic polymer PBO as the model system, we have demonstrated that AuPd alloy NPs are especially

efficient at catalyzing multiple chemical reactions in one pot, including FA dehydrogenation, nitro-hydrogenation, and amine/aldehyde condensation, to form PBO. The AuPd NPs show both size- and composition-dependent catalytic polymerization, and 8-nm Au₃₉Pd₆₁ NPs are the most efficient catalysts for the formation of PBO ($M_w = 3.6$ kDa). The PBO shows excellent thermal stability up to 600°C, which is comparable with the commercial PBO (Zylon, $M_w = 40$ kDa). More importantly, this “lighter” PBO exhibits much improved chemical and mechanical stability compared with Zylon after exposure to water, DMSO, or even 0.5% PA aqueous solution under either ambient or boiling conditions. Our new synthesis solves the long-standing PBO purity and degradation problems by demonstrating that the AuPd NP-catalyzed one-pot reaction is key to obtaining highly pure PBO, and chemical purity is essential for the PBO to maintain its thermomechanical stability. The NP catalyst is stable in the polymerization conditions and can be separated easily from the reaction system and recycled for the next round of reaction. This AuPd alloy NP-catalyzed reaction is not limited to the formation of PBO, and we are actively working to extend this method as a general approach to prepare highly pure rigid organic polymers with more rational control of polymerization for broad ballistic fiber, anti-flame, smart-textile, and ionic separation membrane applications.

EXPERIMENTAL PROCEDURES

Synthesis of 4-nm Au Seeds

HAuCl₄ (0.2 g) was dissolved in 10 mL of tetralin and 10 mL of OAm at 4°C under Ar flow and vigorous magnetic stirring. BBA (0.5 mmol) was dissolved in 1 mL of tetralin and 1 mL of OAm via sonication. The solution was then injected into the HAuCl₄ solution. The mixed solution was then stirred for 1 h at 45°C before 40 mL of acetone was added to collect Au NPs via centrifugation (8,500 rpm, 8 min). The product was dispersed in 20 mL of hexane, precipitated out by adding 40 mL of ethanol and centrifugation, and redispersed in hexane.

Synthesis of 6-nm Au Seeds

HAuCl₄ (0.2 g) was dissolved in 10 mL of tetralin and 10 mL of OAm at 4°C under Ar flow and vigorous magnetic stirring. BBA (0.5 mmol) was dissolved in 1 mL of tetralin and 1 mL of OAm via sonication. The solution was then injected into the HAuCl₄ solution. The mixed solution was then stirred for 1 h at 4°C before 40 mL of acetone was added to collect Au NPs via centrifugation (8,500 rpm, 8 min). The product was dispersed in 20 mL of hexane, precipitated out by adding 40 mL of ethanol and centrifugation, and redispersed in hexane.

Synthesis of 8-nm Au Seeds

30 mg of 6-nm Au NPs was added to a solution made from 10 mL of ODE, 10 mL of OAm, and 0.1 g of HAuCl₄ at room temperature under Ar flow and vigorous magnetic stirring. The reaction solution was then heated to 80°C at 5°C min⁻¹ and kept at this temperature for 2 h. The reaction solution was cooled down to room temperature and the 8-nm Au NP product was separated as described for the synthesis of 6-nm Au NPs.

Synthesis of 10-nm Au Seeds

30 mg of 8-nm Au NPs was added to a solution made from 10 mL of ODE, 10 mL of OAm, and 0.12 g of HAuCl₄ at room temperature under Ar flow and vigorous magnetic stirring. The reaction solution was then heated to 80°C at 5°C min⁻¹ and kept at this temperature for 2 h. The reaction solution was cooled down to room temperature and the 8-nm Au NP product was separated as described for the synthesis of 6-nm Au NPs.

Seed-Mediated Synthesis of Au₃₉Pd₆₁/C from 4 to 10 nm

76 mg of Pd(acac)₂, 15 mL of OAm, and 0.30 mL of OAc were mixed under N₂ at 70°C for 30 min to form a clear solution, then 18 mg of Au seeds from 4 to 10 nm dispersed in 2 mL of hexane was dropped into the solution. The solution was heated to 260°C at 2°C min⁻¹ and kept at 260°C for 1 h before it was cooled to room temperature. The Au₃₉Pd₆₁ NPs were separated by adding 100 mL of ethanol and centrifuging at 9,500 rpm for 8 min. The product was purified by dispersing in hexane and flocculating with ethanol and precipitating by centrifugation (9,500 rpm, 8 min). The purification process was repeated once, and the final NP product was redispersed into hexane for further use. Au₃₉Pd₆₁ NPs (10 mg) were dissolved in hexane in a 100-mL vial and 100 mg of Ketjen carbon support was carefully added. This colloidal mixture was sonicated for 2 h. The reaction mixture was then cooled down to room temperature. Ethanol (120 mL) was added, and the mixture was centrifuged at 8,000 rpm for 8 min. This procedure was repeated twice. The Au₃₉Pd₆₁/C NPs were recovered by adding acetone. Acetone was evaporated and the resultant Au₃₉Pd₆₁/C NPs were weighed, followed by annealing under 95% Ar + 5% H₂ at 500°C for 10 min, which produced Au₃₉Pd₆₁/C NPs with different sizes for further study.

Formic Acid Dehydrogenation

A two-necked reaction flask (25 mL) containing a Teflon-coated stir bar was placed on a magnetic stirrer with a thermostat set to 50.0°C ± 1°C by using a constant-temperature bath. A gas burette filled with water was connected to one neck of the flask (the other neck was sealed) to measure the volume of gas mixture evolved from the reaction. Aqueous suspension of the catalyst (9.64 mL) was transferred into the reaction flask, and 0.36 mL (9 mmol) of FA was added into the stirred (800 rpm) solution. The volume of gas mixture evolved was measured by recording the volume of water displaced. The reaction was considered to cease when gas generation was no longer observed.

TOF Calculation

The turnover frequency reported in herein is an apparent TOF value based on the number of Au and Pd atoms in catalysts, which is calculated from the equation as follows:

$$\text{TOF} = P_0 V / (2RT n_{\text{Au+Pd}} t),$$

where P_0 is the atmospheric pressure, V is the final volume of H₂ + CO₂ gas, R is the universal gas constant, T is the reaction temperature (353 K), $n_{\text{Au+Pd}}$ is the total mole number of Au and Pd atoms in catalyst, and t is the completion time of the reaction. The average TOF of the initial 10 min was adopted for the TOF values.

Bis-Imine Synthesis

To a mixture of 1,5-diisopropoxy-2,4-dinitrobenzene (1 mmol), benzaldehyde (2.1 mmol), NMP (3 mL), FA (10 mmol), and AuPd/C (2.5 mol %) was added. After reacting for 6 h at 80°C, the catalyst was filtered and rinsed with water. The solvent was removed under vacuum and the residue was purified by flash column chromatography (hexane/ethyl acetate = 8:1) to give the bis-imine product. All the catalytic tests were performed under the same metal loading, with variance only in Au, Pd ratio, or nanoparticle size.

Synthesis of 1,5-Diisopropoxy-2,4-Dinitrobenzene

To a mixture of potassium carbonate (5.5 g, 40 mmol) and 2-propanol (40 mL), 1,5-difluoro-2,4 dinitrobenzene (2.04 g, 10 mmol) was added while stirring under nitrogen. After reacting for 2 days at room temperature, a generated precipitate was

filtered and then rinsed several times with water. The obtained solid was dried at 80°C for 12 h in a vacuum to provide a yellow powder (2.243 g, 79%).

Synthesis of Pre-PBO

Under a nitrogen atmosphere, 1,5-diisopropoxy-2,4-dinitrobenzene (0.284 g, 1.0 mmol) was dissolved in NMP (3 mL), to which terephthalaldehyde (0.134 g, 1.0 mmol), FA (10 mmol), and AuPd/C (30 mg, 2.5 mol %) were added, and the mixture was stirred at 80°C for 24 h. After the catalyst was filtered off, the solution was poured into 80 mL of methanol to produce a precipitate, which was filtered and rinsed several times with methanol. The obtained solid was then dried at 80°C for 24 h in a vacuum to produce a dark-purple powder (0.336 g, yield 93%). ¹H-NMR (400 MHz, tetrahydrofuran [THF]-d₈) δ [ppm] = 8.840 (s, 2H), 8.16–8.11 (m, 4H), 6.95 (s, 1H), 6.82 (s, 1H), 4.71–4.64 (m, 2H), 1.41 (d, 12H) (Figure S19). ¹³C-NMR (100 MHz, THF-d₈) δ [ppm] = 151.7, 137.2, 132.5, 129.3, 127.8, 127.2, 127.0, 124.9, 122.4, 72.1, 21.5 (Figure S20).

Conversion of Pre-PBO to PBO

One gram of the pre-PBO was weighed out and heated at 300°C in an annealing oven under a N₂ atmosphere for 6 h to ensure complete conversion to PBO.

Stability Test of the PBO and Zylon at Room Temperature

The PBO (100 mg) and Zylon (100 mg) were immersed in different solvents (10 mL) and stored at room temperature for 1 month. Thereafter, the solid was filtered and dried at 80°C for 24 h under vacuum.

Stability Test of the PBO and Zylon in Boiling Water

The PBO (100 mg) and Zylon (100 mg) were boiled in water at 100°C for 5 days. Thereafter, the solid was filtered and dried at 80°C for 24 h under vacuum.

Fabrication of PBO Films

The PBO or Zylon (500 mg) were dissolved in methanesulfonic acid at 80°C for 5 h. The solution was then cast on a glass substrate to obtain a thin film, which was dried at 80°C for 3 h and 130°C for 3 h. The film was peeled off the glass substrate by immersing the substrate in water. The obtained film was dried at 80°C for 12 h under vacuum for further mechanical tests.

Characterization

Samples for TEM and HRTEM analyses were prepared by depositing a single drop of diluted NP dispersion/suspension on amorphous-carbon-coated copper grids. Images were obtained by a JEOL 2010 transmission electron microscope (200 kV). TEM with a field-emission electron source and STEM analyses were obtained on a Hitachi HD2700C (200 kV) with a probe aberration correction at Brookhaven National Laboratory. X-ray powder diffraction patterns of the samples were collected on a Bruker AXS D8-Advanced diffractometer with Cu K α radiation (λ = 1.5406 Å). The compositions of the NPs were measured by ICP-AES. For ICP-AES analyses, the dried NPs were dissolved in warm aqua regia (~70°C, 30 min) to ensure the complete dissolution of metal into the acid. The solution was then diluted with 2% HNO₃ solution. The measurements were carried out on a JY2000 Ultrace ICP atomic emission spectroscope equipped with a JY-AS 421 autosampler and 2,400 g mm⁻¹ holographic grating. Electrochemical measurements were carried out on an Autolab 302 potentiostat (Eco Chemie, the Netherlands) with GC-RDE (0.196 cm²) as a working electrode, Ag/AgCl (4 M KCl) as a reference electrode, and graphite rod as a counter electrode. The reference electrode was calibrated to RHE before the measurements.

XPS was performed on an ESCA 210 and MICROLAB 310D spectrometer using a Mg KR source. The analyses of products after tandem reactions were carried out by gas chromatography-mass spectrometry (GC-MS) using an Agilent 6890 gas chromatograph coupled to a 5973 mass spectrometer detector with a DB-5 (Agilent) fused silica capillary column (length \times internal diameter 30 m \times 0.25 mm, df 0.25 μ m) and helium as carrier gas. The gas chromatograph was temperature programmed from 65°C (3 min initial time) to 300°C at 6°C min⁻¹ (isothermal for 20 min final time). The mass spectrometer was operated in the electron impact mode at 70 eV ionization energy. Mass spectrometric data were acquired and processed using the GC-MS data system (Agilent Chemstation). Compounds were identified by gas chromatographic retention index and mass spectrum comparison with authentic standards, literature, and library data, and unknown compounds were characterized by interpretation of the fragmentation pattern of their mass spectra. A TGA/DSC 1 STARe System from Mettler Toledo provided with a horizontal balance was used to measure the thermal stability. Approximately 10 mg of sample was placed in an alumina pan and heated from 100°C to 900°C or 300°C to 900°C with an 80-mL min⁻¹ nitrogen purge and heating rate of 10°C min⁻¹. The change in weight was continuously registered. The tensile strength of sample films was tested with a constant span length of 5 cm using upper/lower grips (Instron 2714-006) on an Instron 5942 load frame. Load was applied by moving the crosshead at a rate of 0.1 mm min⁻¹ while measuring the force with a 500-N load cell (Instron 2580-105). The tensile strength was evaluated from the breaking load, the width of the specimen, and its thickness. GPC was performed using an Agilent 1260 equipped with two Poroshell 120 EC-C18 columns heated at 35°C (4.6 \times 100 mm, 2.7 μ m) and a UV-vis diode-array detector and refractive detector. The eluent was inhibitor-free THF, and the system was calibrated with standard polystyrene standards ranging from 580 to 1,500,000 Da. UV-vis absorption spectra were measured using an Agilent Technologies Cary 5000 UV-Vis Spectrophotometer. PBO samples were dissolved in methanesulfonic acid (MSA) (concentration 7 \times 10⁻⁶ g mL⁻¹) for the measurements. The solution PL measurements were performed on an Edinburgh Instruments Fluorescence Spectrometer FS5. The samples were dissolved in MSA for measurements. The PL measurements were employed with excitation at 335 nm for monomer and 365 nm for dimer, tetramer, PBO, and Zylon.

DFT Calculation

DFT calculations were performed using the Vienna Ab Initio Simulation Package¹ with the projector-augmented wave pseudopotentials.² The exchange-correlation interaction was described by Perdew-Burke-Ernzerhof functional.³ A plane-wave energy cutoff of 400 eV was used for all calculations. The Au/Pd (111) surface for FA dehydrogenation was modeled by a four-atomic-layer slab (64 atoms). For the hydrogenation of nitro groups and the condensation of amino and carbonyl groups, a three-atomic-layer slab (144 atoms) was adopted. The adjacent computational slabs were separated by a 15-Å vacuum in the normal direction of the surface. The atoms in the top two layers were fully relaxed while the rest of the atoms were fixed in the equilibrium positions. The Brillouin zone was sampled with a 3 \times 3 \times 1 *k*-mesh according to the Monkhorst-Pack scheme.⁴ The free energy of reaction intermediate was calculated as

$$G = E_{\text{DFT}} + \text{ZPE} + \int C_p dT - TS, \quad (\text{Equation 1})$$

where E_{DFT} is the total energy of the surface with the intermediate; ZPE, C_p , and $-TS$ are the zero-point energy, heat capacity, and entropy corrections calculated on the basis of the molecular vibration analysis at $T = 300$ K.⁵ We assume that any changes in the vibrations of the metal surface caused by the adsorbate are minimal.

SUPPLEMENTAL INFORMATION

Supplemental Information can be found online at <https://doi.org/10.1016/j.matt.2019.09.001>.

ACKNOWLEDGMENTS

The work at Brown University was supported in part by the US Army Research Laboratory and the US Army Research Office under grant W911NF-15-1-0147, Strem Chemicals, the Office of Vice President of Research of Brown University, and the Institute of Molecular and Nanoscale Innovation of Brown University. M.M. is supported by the National Science Foundation Graduate Research Fellowship under grant no. 1644760. The work at California State University Northridge was supported by the National Science Foundation PREM program (DMR-1828019). The electron microscopy work used resources of the Center for Functional Nanomaterials, which is a US DOE Office of Science Facility, at Brookhaven National Laboratory under contract no. DE-SC0012704. Zylon was generously supplied by Toyobo (USA).

AUTHOR CONTRIBUTIONS

S.S., C.T.S., C.Y., and X.G. designed and studied reactions and polymer formation and wrote the manuscript. Z.Y. synthesized AuPd NPs. Z.Z. and G.L. performed DFT calculations. X.L. and D.S. performed TEM and elemental analyses. M.M. and M.S. performed control experiments and confirmed the reproducibility of the new synthesis. Y.Y., J.W., J.R., and O.C. performed fluorescence and GPC characterizations of PBO. C.J.C., J.A., and P.G. conducted the mechanical tests on PBO films. All authors discussed the results and commented on the manuscript.

DECLARATION OF INTERESTS

The authors declare no competing interests.

Received: June 6, 2019

Revised: August 8, 2019

Accepted: September 3, 2019

Published: October 9, 2019

REFERENCES

1. Yang, Y., Luo, M.C., Zhang, W.Y., Sun, Y.J., Chen, X., and Guo, S.J. (2018). Metal surface and interface energy electrocatalysis: fundamentals, performance engineering, and opportunities. *Chem* 4, 2054–2083.
2. Vasileff, A., Xu, C.C., Jiao, Y., Zheng, Y., and Qiao, S.Z. (2018). Surface and interface engineering in copper-based bimetallic materials for selective CO₂ electroreduction. *Chem* 4, 1809–1831.
3. Nai, J.W., Zhang, J.T., and Lou, X.W. (2018). Construction of single-crystalline prussian blue analog hollow nanostructures with tailorable topologies. *Chem* 4, 1967–1982.
4. Fenton, J.L., Steimle, B.C., and Schaak, R.E. (2018). Tunable intraparticle frameworks for creating complex heterostructured nanoparticle libraries. *Science* 360, 513–517.
5. Chen, P.Z., Pollit, L., Jones, L., and Gu, F.X. (2018). Functional two- and three-dimensional architectures of immobilized metal nanoparticles. *Chem* 4, 2301–2328.
6. Wang, G.Q., Liu, Y.D., Gao, C.B., Guo, L., Chi, M.F., Ijiri, K., Maeda, M., and Yin, Y.D. (2017). Island growth in the seed-mediated overgrowth of monometallic colloidal nanostructures. *Chem* 3, 678–690.
7. Zhang, C., Macfarlane, R.J., Young, K.L., Choi, C.H.J., Hao, L.L., Auyeung, E., Liu, G.L., Zhou, X.Z., and Mirkin, C.A. (2013). A general approach to DNA-programmable atom equivalents. *Nat. Mater.* 12, 741–746.
8. Yavuz, M.S., Cheng, Y.Y., Chen, J.Y., Cobley, C.M., Zhang, Q., Rycenga, M., Xie, J.W., Kim, C., Song, K.H., Schwartz, A.G., et al. (2009). Gold nanocages covered by smart polymers for controlled release with near-infrared light. *Nat. Mater.* 8, 935–939.
9. Wu, C.H., Liu, C., Su, D., Xin, H.L.L., Fang, H.T., Erens, B., Zhang, S., Murray, C.B., and Salmeron, M.B. (2019). Bimetallic synergy in cobalt-palladium nanocatalysts for CO oxidation. *Nat. Catal.* 2, 78–85.
10. Wang, H., Liu, R.P., Li, Y.T., Lu, X.J., Wang, Q., Zhao, S.Q., Yuan, K.J., Cui, Z.M., Li, X., Xin, S., et al. (2018). Durable and efficient hollow porous oxide spinel microspheres for oxygen reduction. *Joule* 2, 337–348.
11. Tsumori, N., Chen, L.Y., Wang, Q.J., Zhu, Q.L., Kitta, M., and Xu, Q. (2018). Quasi-MOF: exposing inorganic nodes to guest metal nanoparticles for drastically enhanced catalytic activity. *Chem* 4, 845–856.
12. Liu, Y.W., Xiao, C., Huang, P.C., Cheng, M., and Xie, Y. (2018). Regulating the charge and spin ordering of two-dimensional ultrathin solids for electrocatalytic water splitting. *Chem* 4, 1263–1283.
13. Cao, S., Chen, Y., Wang, H., Chen, J., Shi, X.H., Li, H.M., Cheng, P., Liu, X.F., Liu, M., and Piao, L.Y. (2018). Ultrasmall CoP nanoparticles as efficient cocatalysts for photocatalytic formic acid dehydrogenation. *Joule* 2, 549–557.
14. Sun, Q.M., Wang, N., Bing, Q.M., Si, R., Liu, J.Y., Bai, R.S., Zhang, P., Jia, M.J., and Yu, J.H.

- (2017). Subnanometric hybrid Pd-M(OH)(2), M=Ni, Co, clusters in zeolites as highly efficient nanocatalysts for hydrogen generation. *Chem* 3, 477–493.
15. Hu, C.Y., Ma, Q.Y., Hung, S.F., Chen, Z.N., Ou, D.H., Ren, B., Chen, H.M., Fu, G., and Zheng, N.F. (2017). In situ electrochemical production of ultrathin nickel nanosheets for hydrogen evolution electrocatalysis. *Chem* 3, 122–133.
16. Wang, H.W., Gu, X.K., Zheng, X.S., Pan, H.B., Zhu, J.F., Chen, S., Cao, L.N., Li, W.X., and Lu, J.L. (2019). Disentangling the size-dependent geometric and electronic effects of palladium nanocatalysts beyond selectivity. *Sci. Adv.* 5, eaat6413.
17. Yu, C., Guo, X.F., Shen, M.Q., Shen, B., Muzzio, M., Yin, Z.Y., Li, Q., Xi, Z., Li, J.R., Seto, C.T., et al. (2018). Maximizing the catalytic activity of nanoparticles through monolayer assembly on nitrogen-doped graphene. *Angew. Chem. Int. Ed.* 57, 451–455.
18. Tao, H.C., Choi, C., Ding, L.X., Jiang, Z., Hang, Z.S., Jia, M.W., Fan, Q., Gao, Y.N., Wang, H.H., Robertson, A.W., et al. (2019). Nitrogen fixation by Ru single-atom electrocatalytic reduction. *Chem* 5, 204–214.
19. Li, Z.L., Qu, Y.Z., Wang, J.J., Liu, H.L., Li, M.R., Miao, S., and Li, C. (2019). Highly selective conversion of carbon dioxide to aromatics over tandem catalysts. *Joule* 3, 570–583.
20. Zhao, X.J., Zhou, L.Y., Zhang, W.Y., Hu, C.Y., Dai, L., Ren, L.T., Wu, B.H., Fu, G., and Zheng, N.F. (2018). Thiol treatment creates selective palladium catalysts for semihydrogenation of internal alkynes. *Chem* 4, 1080–1091.
21. Tian, S.B., Fu, Q., Chen, W.X., Feng, Q.C., Chen, Z., Zhang, J., Cheong, W.C., Yu, R., Gu, L., Dong, J.C., et al. (2018). Carbon nitride supported Fe₂ cluster catalysts with superior performance for alkene epoxidation. *Nat. Commun.* 9, 2353.
22. Tao, L., Yan, T.H., Li, W.Q., Zhao, Y., Zhang, Q., Liu, Y.M., Wright, M.M., Li, Z.H., He, H.Y., and Cao, Y. (2018). Toward an integrated conversion of 5-hydroxymethylfurfural and ethylene for the production of renewable p-Xylene. *Chem* 4, 2212–2227.
23. Peng, Y.H., Wang, L.B., Luo, Q.Q., Cao, Y., Dai, Y.Z., Li, Z.L., Li, H.L., Zheng, X.S., Yan, W.S., Yang, J.L., et al. (2018). Molecular-level insight into how hydroxyl groups boost catalytic activity in CO₂ hydrogenation into methanol. *Chem* 4, 613–625.
24. Yu, C., Guo, X.F., Shen, B., Xi, Z., Li, Q., Yin, Z.Y., Liu, H., Muzzio, M., Shen, M.Q., Li, J.R., et al. (2018). One-pot formic acid dehydrogenation and synthesis of benzene-fused heterocycles over reusable AgPd/WO_{2.72} nanocatalyst. *J. Mater. Chem. A* 6, 23766–23772.
25. Gao, W., Gao, R., Zhao, Y.F., Peng, M., Song, C.Q., Li, M.Z., Li, S.W., Liu, J.J., Li, W.Z., Deng, Y.C., et al. (2018). Photo-driven syngas conversion to lower olefins over oxygen-decorated Fe₅C₂ catalyst. *Chem* 4, 2917–2928.
26. Lin, H., Huang, Y.D., and Wang, F. (2008). Synthesis and properties of poly(p-(2,5-dihydroxy)-phenylenebenzobisoxazole) fiber. *Int. J. Mol. Sci.* 9, 2159–2168.
27. Afshari, M., Sikkema, D.J., Lee, K., and Bogle, M. (2008). High performance fibers based on rigid and flexible polymers. *Polym. Rev.* 48, 230–274.
28. Hu, X.D., Jenkins, S.E., Min, B.G., Polk, M.B., and Kumar, S. (2003). Rigid-rod polymers: synthesis, processing, simulation, structure, and properties. *Macromol. Mater. Eng.* 288, 823–843.
29. So, Y.H., Heeschen, J.P., Bell, B., Bonk, P., Briggs, M., and DeCaire, R. (1998). Study of the mechanism for poly(p-phenylene)benzoxazole polymerization—a remarkable reaction pathway to make rigid-rod polymers. *Macromolecules* 31, 5229–5239.
30. Luo, S.J., Zhang, Q.N., Zhu, L.X., Lin, H.Q., Kazanowska, B.A., Doherty, C.M., Hill, A.J., Gao, P.Y., and Guo, R.L. (2018). Highly selective and permeable microporous polymer membranes for hydrogen purification and CO₂ removal from natural gas. *Chem. Mater.* 30, 5322–5332.
31. Hao, X.M., Zhu, J., Jiang, X., Wu, H.T., Qiao, J.S., Sun, W., Wang, Z.H., and Sun, K.N. (2016). Ultrastrong polyoxazole nanofiber membranes for dendrite-proof and heat-resistant battery separators. *Nano Lett.* 16, 2981–2987.
32. Kolhe, N.B., Asha, S.K., Senanayak, S.P., and Narayan, K.S. (2010). n-Type field effect transistors based on rigid rod and liquid crystalline alternating copoly(benzobisoxazole) imides containing perylene and/or naphthalene. *J. Phys. Chem. B* 114, 16694–16704.
33. Park, H.B., Jung, C.H., Lee, Y.M., Hill, A.J., Pas, S.J., Mudie, S.T., Van Wagner, E., Freeman, B.D., and Cookson, D.J. (2007). Polymers with cavities tuned for fast selective transport of small molecules and ions. *Science* 318, 254–258.
34. Kanbargi, N., Hu, W.G., and Lesser, A.J. (2017). Degradation mechanism of poly(p-phenylene-2,6-benzobisoxazole) fibers by P-31 solid-state NMR. *Polym. Degrad. Stabil.* 136, 131–138.
35. Froimowicz, P., Zhang, K., and Ishida, H. (2016). Intramolecular hydrogen bonding in benzoxazines: when structural design becomes functional. *Chemistry* 22, 2691–2707.
36. Park, E.S., Sieber, J., Guttman, C., Rice, K., Flynn, K., Watson, S., and Holmes, G. (2009). Methodology for detecting residual phosphoric acid in polybenzoxazole fibers. *Anal. Chem.* 81, 9607–9617.
37. Yang, Y., Xu, H., Cao, D., Zeng, X.C., and Cheng, D. (2019). Hydrogen production via efficient formic acid decomposition: engineering the surface structure of Pd-based alloy catalysts by design. *ACS Catal.* 9, 781–790.
38. Yu, W.Y., Mullen, G.M., Flaherty, D.W., and Mullins, C.B. (2014). Selective hydrogen production from formic acid decomposition on Pd-Au bimetallic surfaces. *J. Am. Chem. Soc.* 136, 11070–11078.
39. Muzzio, M., Yu, C., Lin, H.H., Yom, T., Boga, D.A., Xi, Z., Li, N., Yin, Z.Y., Li, J.R., Dunn, J.A., et al. (2019). Reductive amination of ethyl levulinate to pyrrolidones over AuPd nanoparticles at ambient hydrogen pressure. *Green. Chem.* 21, 1895–1899.
40. Gu, X., Lu, Z.H., Jiang, H.L., Akita, T., and Xu, Q. (2011). Synergistic catalysis of metal-organic framework-immobilized Au-Pd nanoparticles in dehydrogenation of formic acid for chemical hydrogen storage. *J. Am. Chem. Soc.* 133, 11822–11825.
41. Zhu, W., Michalsky, R., Metin, O., Lv, H., Guo, S., Wright, C.J., Sun, X., Peterson, A.A., and Sun, S. (2013). Monodisperse Au nanoparticles for selective electrocatalytic reduction of CO₂ to CO. *J. Am. Chem. Soc.* 135, 16833–16836.
42. Fukumaru, T., Saegusa, Y., Fujigaya, T., and Nakashima, N. (2014). Fabrication of poly(p-phenylenebenzobisoxazole) film using a soluble poly(o-alkoxyphenylamide) as the precursor. *Macromolecules* 47, 2088–2095.
43. Feng, D.D., Wang, S.F., Zhuang, Q.X., Guo, P.Y., Wu, P.P., and Han, Z.W. (2004). Joint theoretical and experimental study of the UV absorption spectra of polybenzoxazoles. *J. Mol. Struct.* 707, 169–177.
44. DiCesare, N., Belletete, M., Leclerc, M., and Durocher, G. (1999). Intermolecular interactions in conjugated oligothiophenes. 2. Quantum chemical calculations performed on crystalline structures of terthiophene and substituted terthiophenes. *J. Phys. Chem. A* 103, 803–811.
45. Yoo, J.S., Zhao, Z.J., Nørskov, J.K., and Studt, F. (2015). Effect of boron modifications of palladium catalysts for the production of hydrogen from formic acid. *ACS Catal.* 5, 6579–6586.
46. Zhou, X.W., Johnson, R.A., and Wadley, H.N.G. (2004). Misfit-energy-increasing dislocations in vapor-deposited CoFe/NiFe multilayers. *Phys. Rev. B* 69, 144113.
47. Ruban, A., Hammer, B., Stoltze, P., Skriver, H.L., and Nørskov, J.K. (1997). Surface electronic structure and reactivity of transition and noble metals. *J. Mol. Catal. A Chem.* 115, 421–429.

Matter, Volume 1

Supplemental Information

Highly Efficient AuPd Catalyst for Synthesizing Polybenzoxazole with Controlled Polymerization

Chao Yu, Xuefeng Guo, Zhouyang Yin, Zhonglong Zhao, Xing Li, Jerome Robinson, Michelle Muzzio, Cintia J. Castilho, Mengqi Shen, Yucheng Yuan, Junyu Wang, John Antolik, Gang Lu, Dong Su, Ou Chen, Pradeep Guduru, Christopher T. Seto, and Shouheng Sun

Supplemental Information

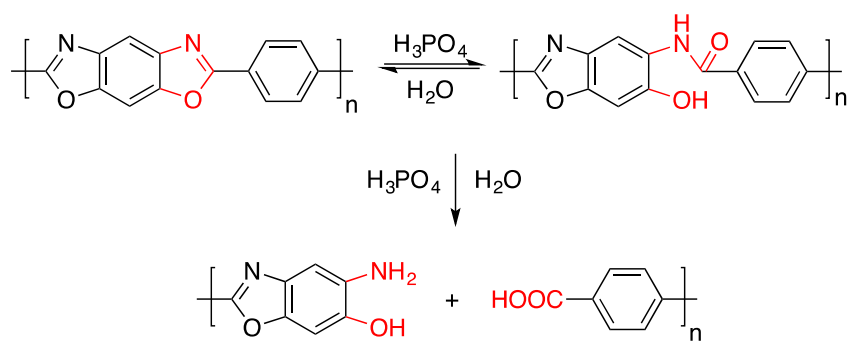


Figure S1. Hydrolysis and ring opening of benzoxazole catalyzed by phosphoric acid.

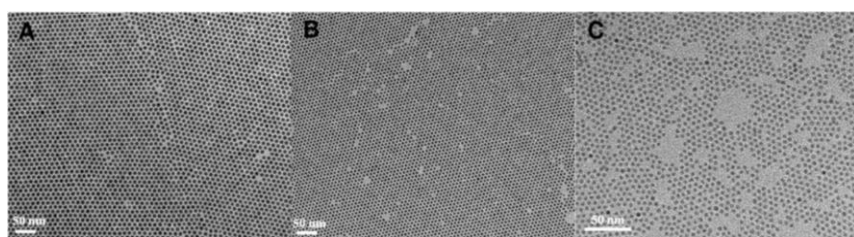


Figure S2. TEM images of Au NPs. (A) 10 nm. (B) 6 nm. (C) 4 nm.

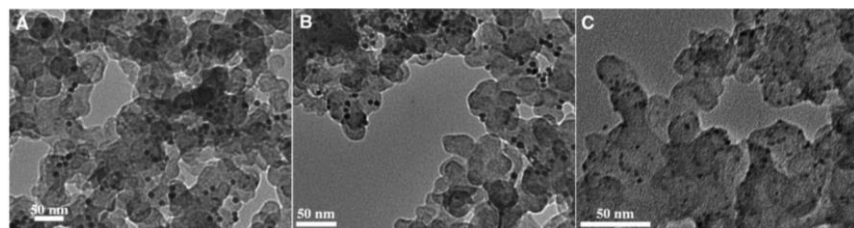


Figure S3. TEM images of Au₃₉Pd₆₁/C with different NP sizes. (A) 10.5±0.2 nm. (B) 6.4±0.3 nm. (C) 4.3±0.2 nm.

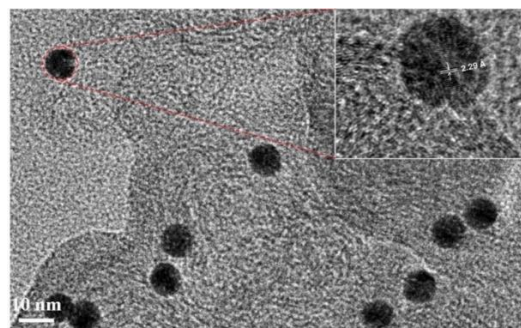


Figure S4. HRTEM image of as-prepared Au₃₉Pd₆₁ NPs.

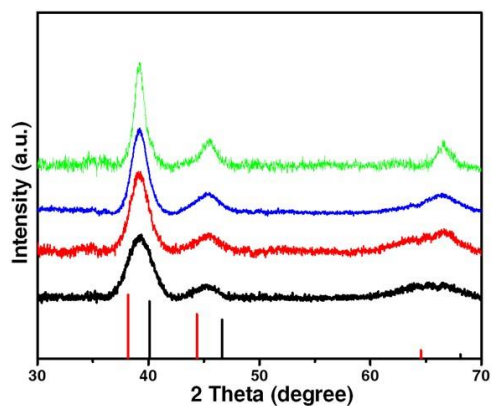


Figure S5. XRD patterns of $\text{Au}_{39}\text{Pd}_{61}/\text{C}$ with four different NP sizes of 10 nm (Green), 8 nm (Blue), 6 nm (Red) and 4 nm (Black).

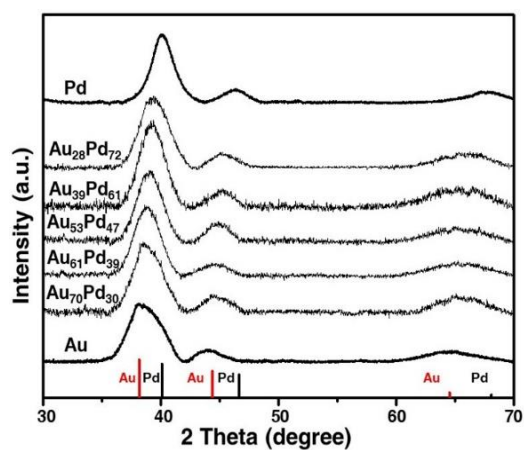


Figure S6. XRD patterns of AuPd NPs with different Au/Pd compositions.

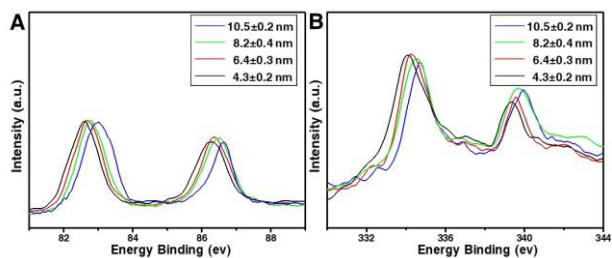


Figure S7. XPS of (A) Au 4f and (B) Pd 3d of $\text{Au}_{39}\text{Pd}_{61}$ NPs of different sizes from 4 to 10 nm.

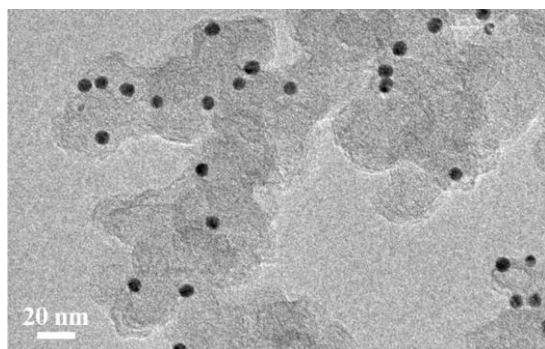


Figure S8. TEM image of 8 nm AuPd after polymerization.

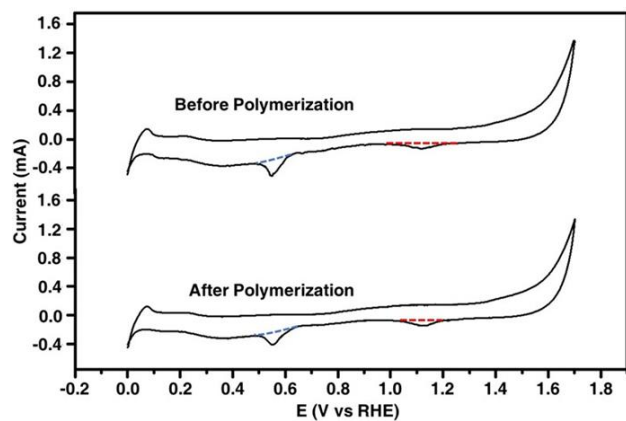


Figure S9. CV of AuPd NPs before and after polymerization reaction. The I-V curves were obtained in 0.5 M H_2SO_4 with a scan rate of 50 mV/s.

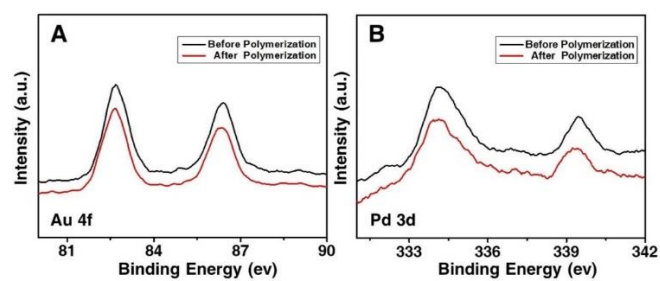


Figure S10. XPS of (A) Au 4f and (B) Pd 3d of 8 nm $\text{Au}_{39}\text{Pd}_{61}$ NPs before and after polymerization reaction.

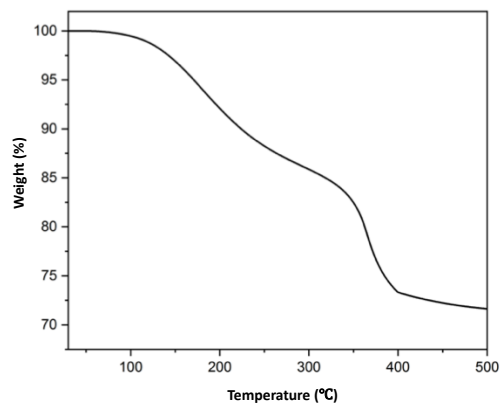


Figure S11. TGA data of pre-PBO prepared from one-pot reaction catalyzed by 8 nm $\text{Au}_{39}\text{Pd}_{61}/\text{C}$.

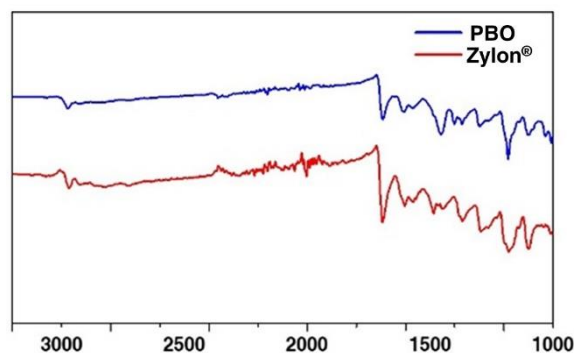


Figure S12. FT-IR spectra of PBO and Zylon®.

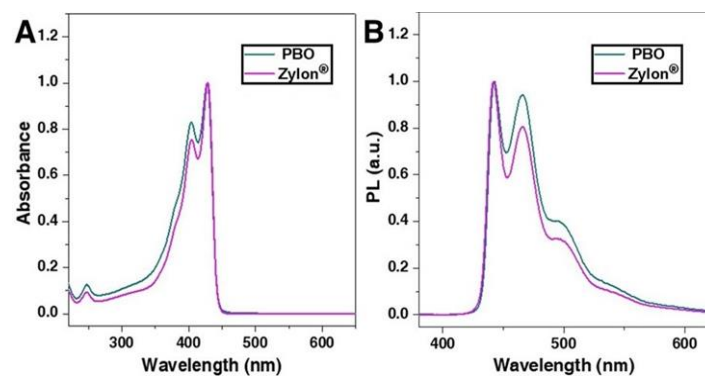


Figure S13. (A) Absorption and (B) PL spectra of PBO and Zylon® in methane sulfonic acid (7×10^{-6} g/mL).

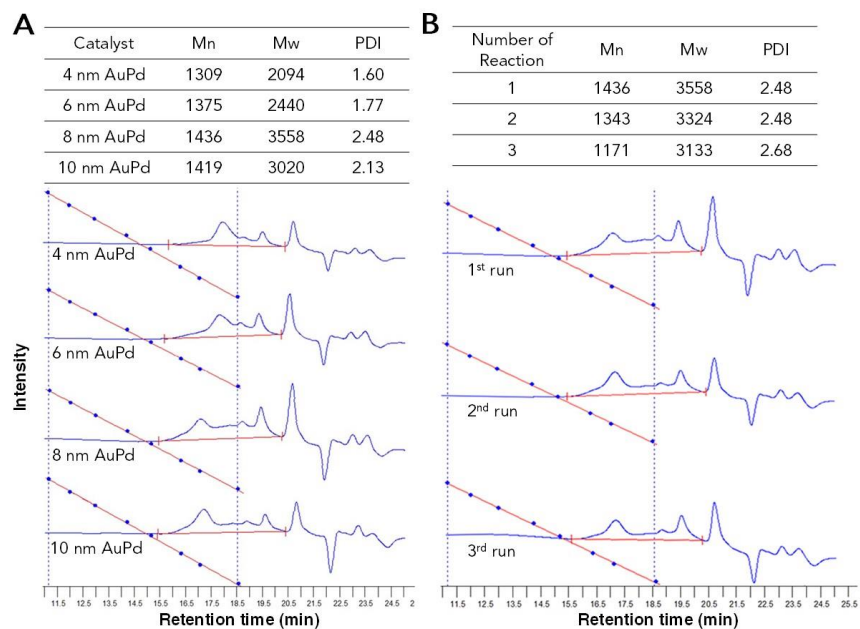


Figure S14. (A) The GPC chromatograms of pre-PBOs formed using different sizes of AuPd NPs. (B) The GPC chromatograms of pre-PBOs formed in three consecutive reactions by using same batch of 8 nm AuPd catalyst.

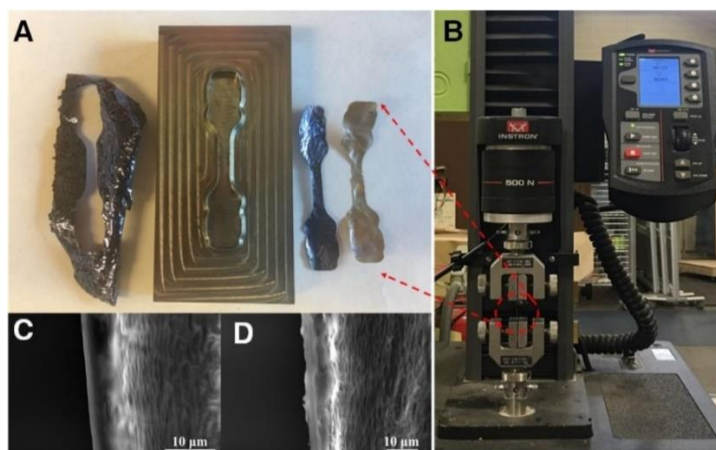


Figure S15. (A) The customized cutter for PBO samples. (B) The testing system for PBO samples. (C) SEM image of the PBO sample. (D) SEM image of the Zylon[®] sample.

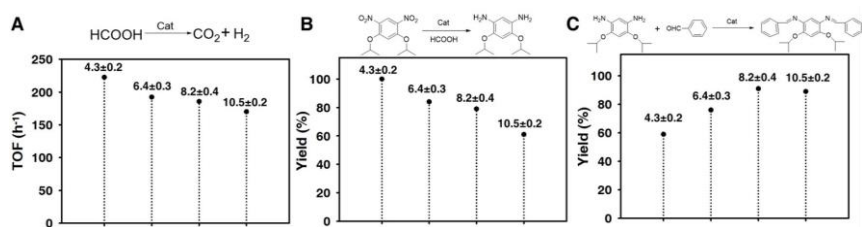


Figure S16. (A) The TOF values for FA dehydrogenation catalyzed by Au₃₉Pd₆₁/C with AuPd in four different sizes: 10, 8, 6 and 4 nm. Reaction conditions: Au₃₉Pd₆₁/C (2.5 mol%), NMP (3 mL), and FA (10 mmol), 80 °C, 1 h. (B) The AuPd NP size dependent yields of 1,5-diisopropoxy-2,4-diaminobenzene synthesized by the Au₃₉Pd₆₁/C-catalyzed dehydrogenation of FA and the hydrogenation of 1,5-diisopropoxy-2,4-dinitrobenzene. Reaction conditions: Au₃₉Pd₆₁/C (2.5 mol%), 1,5-diisopropoxy-2,4-dinitrobenzene (1 mmol), NMP (3 mL), and FA (10 mmol), 80 °C, 2 h. (C) The AuPd NP size dependent yields of bis-imine formed by the Au₃₉Pd₆₁/C-catalyzed condensation of 1,5-diisopropoxy-2,4-diaminobenzene and benzaldehyde. Reaction conditions: Au₃₉Pd₆₁/C (2.5 mol%), 1,5-diisopropoxy-2,4-diaminobenzene (1 mmol), benzaldehyde (2.1 mmol), NMP (3 mL), 80 °C, 3 h.

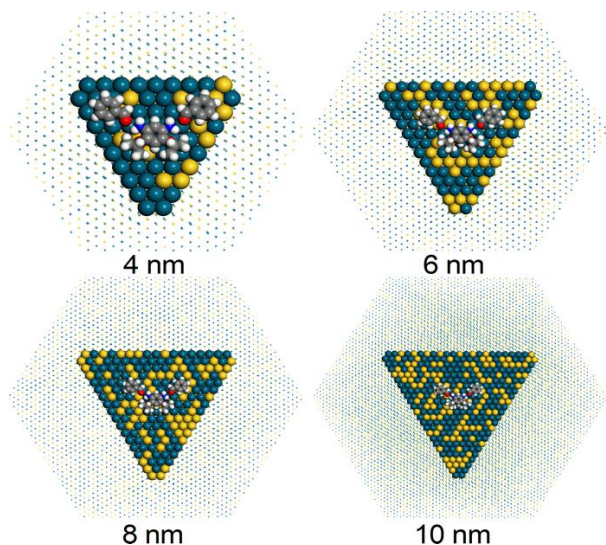


Figure S17. Atomic structures of the DFT optimized amino and carbonyl groups on the MM optimized AuPd TO (111) surfaces. Yellow, cyan, gray, blue, red, and white spheres represent Au, Pd, C, N, O, and H atoms, respectively.

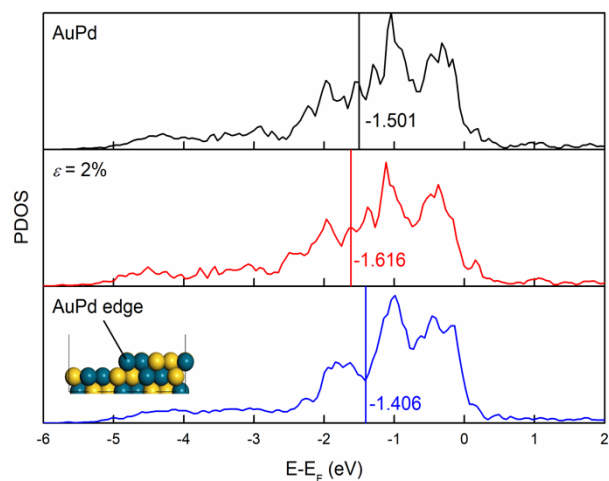


Figure S18. The calculated density of states of the *d*-band of the surface Pd atom for the AuPd (111), AuPd (111) under 2% compression, and the AuPd edge. The vertical solid lines indicate the *d*-band centers. The atomic model for the AuPd edge is shown in the inset: yellow and cyan spheres represent Au and Pd atoms, respectively.

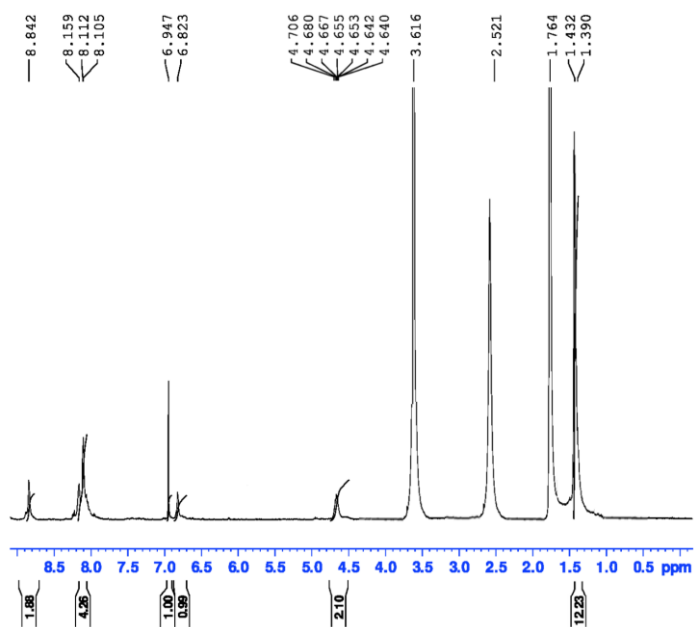


Figure S19. ^1H -NMR (400 MHz, THF-d_8) for pre-PBO.



Size of Au ₃₉ Pd ₆₁	XPS	
	Au (at %)	Pd (at %)
4 nm	39.6	60.4
6 nm	42.7	57.3
8 nm	41.6	58.4
10 nm	37.9	62.1

Sample	ICP		XPS		Electrochemistry	
	Au (at %)	Pd (at %)	Au (at %)	Pd (at %)	Au (at %)	Pd (at %)
8 nm AuPd	39.1	60.9	38.8	61.2	41.0	59.0
8 nm AuPd (after reaction)	37.8	62.2	39.5	60.5	40.2	59.8

Entry	Conditions	Yields (%)
1	No HCOOH, No AuPd/C	15
2	HCOOH, No AuPd/C	35
3	AuPd/C, No HCOOH	91

References

1. Kresse, G. and Furthmüller, J. (1996). Efficient iterative schemes for *ab initio* total-energy calculations using a plane-wave basis set. Phys. Rev. B 54, 11169-11186.
2. Blöchl, P. E. (1994). Projector augmented-wave method. Phys. Rev. B 50, 17953-17979.
3. Perdew, J. P., Burke, K., and Ernzerhof, M. (1996). Generalized Gradient Approximation Made Simple. Phys. Rev. Lett. 77, 3865-3868.
4. Monkhorst, H. J., Pack, J. D. (1976). Special points for Brillouin-zone integrations. Phys. Rev. B 13, 5188-5192.
5. Cramer, C. J. (Wiley, 2004). *Essentials of Computational Chemistry: Theories and Models*. 2nd edn.